Electroosmotic Coupling in Porous Media, a New Model Based on a Fractal Upscaling Procedure

Luong Duy Thanh, Damien Jougnot, Phan van Do, Aida Mendieta, Nguyen Xuan Ca, Vu Xuan Hoa, Pham Minh Tan, Nguyen Thi Hien

To cite this version:

Luong Duy Thanh, Damien Jougnot, Phan van Do, Aida Mendieta, Nguyen Xuan Ca, et al.. Electroosmotic Coupling in Porous Media, a New Model Based on a Fractal Upscaling Procedure. Transport in Porous Media, 2020, 134 (1), pp.249-274. 10.1007/s11242-020-01444-7 . hal-02950764

HAL Id: hal-02950764
https://hal.sorbonne-universite.fr/hal-02950764v1

Electroosmotic coupling in porous media, a new model based on a fractal upscaling procedure

Luong Duy Thanh[a], Damien Jougnot[b], Phan Van Do[a], Aida Mendieta[b],
Nguyen Xuan Ca[c], Vu Xuan Hoa[c], Pham Minh Tan[d], Nguyen Thi Hien[e,f,*]

[a]*Thuyloi University, 175 Tay Son, Dong Da, Hanoi, Vietnam*

[b]*Sorbonne Universit´e, CNRS, EPHE, UMR 7619 Metis, F-75005, Paris, France*

[c]*Faculty of Physics and Technology, TNU-University of Sciences, Thai Nguyen, Vietnam*

[d]*Faculty of Fundamental Sciences, Thai Nguyen University of Technology, Thai Nguyen, Vietnam*

[e]*Ceramics and Biomaterials Research Group, Advanced Institute of Materials Science, Ton Duc Thang University, Ho Chi Minh City, Vietnam*

[f]*Faculty of Applied Sciences, Ton Duc Thang University, Ho Chi Minh City, Vietnam*

Abstract

Electrokinetic and electroosmotic couplings can play important roles in water and ions transport in charged porous media. Electroosmosis is the phenomena explaining the water movement in a porous medium subjected to an electrical field. In this work, a new model is obtained through a new up-scaling procedure, considering the porous medium as a bundle of tortuous capillaries of fractal nature. From the model, the expressions for the electroosmosis pressure coefficient, the relative electroosmosis pressure coefficient, the maximum back pressure, the maximum flow rate, the flow rate-applied back pressure relation and the product of the permeability and formation factor of porous media are also obtained. The sensitivity of the relative electroosmosis pressure coefficient is then analyzed and explained. The model predictions are then successfully compared with published datasets. Additionally, we deduce an expression for the relative streaming potential coefficient and then compare it with a previously published model and experimental data from a dolomite rock sample. We find a good agreement between those models and experimental data, opening up new perspectives to model electroosmotic phenomena in porous media saturated with various fluids.

Keywords: Electroosmosis; Electrokinetics; Water saturation; Zeta potential; Fractal; Porous media

1. Introduction

Electroosmosis is one of the effects of electrokinetic phenomena that occur in porous media with surface charges when filled with one or more fluids containing charged particles. It arises due to the induced movement of a liquid by a voltage across a porous sample and is directly linked to an electrical double layer between the solid grain surface and the pore solution. Electroosmosis has been studied both experimentally and theoretically for a long time (e.g., Reuss, 1809; Quincke, 1861; Smoluchowski, 1902; Nourbehecht, 1963; Lyklema, 1995). Electroosmotic flow is a critical phenomenon that is used in a variety of applications. For example, electroosmotic flow pumps have been used in different fields of microfluidics such as biological and chemical analysis (Good et al., 2006), liquid drug reagent injection/delivery (e.g., Tsai & Sue, 2007; Wang et al., 2009), microelectronic chip cooling (e.g., Linan Jiang et al., 2002; Singhal et al., 2004) and microfluidic devices (e.g., Hu & Li, 2007; Bruus, 2008; Kirby, 2010). Solutes and nonaqueous phase liquids/dense nonaqueous phase liquids can be removed by an electroosmotic technique in the vadose zone for remediation purposes (e.g., Bruell et al., 1992; Wise & Trantolo, 1994; Han et al., 2004; Reddy et al., 1997). Additionally, electroosmosis has great potential for the dewatering of earth masonry structures (e.g., Casagrande, 1983; Lockhart & Hart, 1988; Larue et al., 2006) or drying moisture ingress in existing buildings, stone and earth masonry structures (e.g., Lockhart & Hart, 1988; Ottosen & Rörig-Dalgaard, 2006; Bertolini et al., 2009).

Many studies on electroosmosis flow reported in the literature use cylindrical capillaries or microchannels between two parallel plates (e.g., Rice & Whitehead, 1965; Levine et al., 1975; Olivares et al., 1980; Ohshima & Kondo, 1990; Mohiuddin Mala et al., 1997; Vennela et al., 2011). In

---

*Corresponding author
Email address: nguyenthihien@tdtu.edu.vn (Nguyen Thi Hien)

June 26, 2020

porous media, electroosmotic flow has been presented using capillary bundle models with different capillary geometry such as rectangular, cylindrical and annular geometries (e.g., Wu & Papadopoulos, 2000; Pascal et al., 2012). Bandopadhyay et al. (2013) introduced the parameter of the electro-permeability that relates the flow rate with the applied voltage in porous media. Based on the electroosmotic flow in a single capillary, models for the height difference between the U-tube experiment caused by electroosmosis in a fully saturated porous medium were presented (e.g., Paillat et al., 2000; Liang et al., 2015). For characterization of electroosmotic miropumps fabricated by packing nonporous silica particles, a bundle of capillary tubes model was applied (e.g., Zeng et al., 2001; Yao & Santiago, 2003). Besides capillary tubes models, other approaches based on volume-averaging upscaling can be also applied to calculate the electrokinetic coupling in porous media (e.g., Pride, 1994; Revil & Linde, 2006; Revil et al., 2007).

It has been shown that natural porous media have fractal properties. Their pore space is statistically self-similar over several length scales (among many others, see Mandelbrot, 1982; Katz & Thompson, 1985; Yu & Cheng, 2002). Theory on the fractal nature of porous media has attracted much attention in different areas (e.g., Mandelbrot, 1982; Feder & Aharony, 1989). Therefore, models based on the fractal theory have been applied to study phenomena in both fully and partially saturated porous media (e.g., Cai et al., 2012a,b; Liang et al., 2014; Guarracino & Jougnot, 2018; Soldi et al., 2019; Thanh et al., 2018, 2019). However, to the best of our knowledge, the fractal theory has not yet been used to study electroosmosis in a porous medium under water saturated and partially saturated conditions.

In this work, we apply fractal theory in porous media to obtain a mechanistic analytical model to describe electroosmotic flow in porous media using a capillary tube model. From the derived model, the expressions for the electroosmotic pressure coefficient, the relative electroosmosis pressure coefficient, the maximum back pressure, the maximum flow rate, the flow rate-applied back pressure relation and the product of the formation factor and permeability of porous media are also obtained. To validate the model, the sensitivity of the relative electroosmosis pressure coefficient K_E^r to irreducible water saturation S_{irr}, ratio of the minimum pore radius to the maximum pore radius α and fractal dimension for pore space D_f is analyzed and explained. The model is then compared with published results in both cases of full saturation and partial saturation. Additionally, the expression for the relative streaming potential coefficient K_S^r is also deduced from K_E^r. From that, the change of the relative streaming potential coefficient K_S^r with the water saturation is predicted and compared with another model and with experimental data for a dolomile rock sample available in literature.

2. Theoretical background of electroosmosis

2.1. Theory of electroosmosis

Porous media are constituted by minerals (e.g., silicates, oxides, carbonates) or other materials (e.g., polymers, biological materials) that are generally electrically charged due to isomorphic substitutions (e.g., Hunter, 1981;

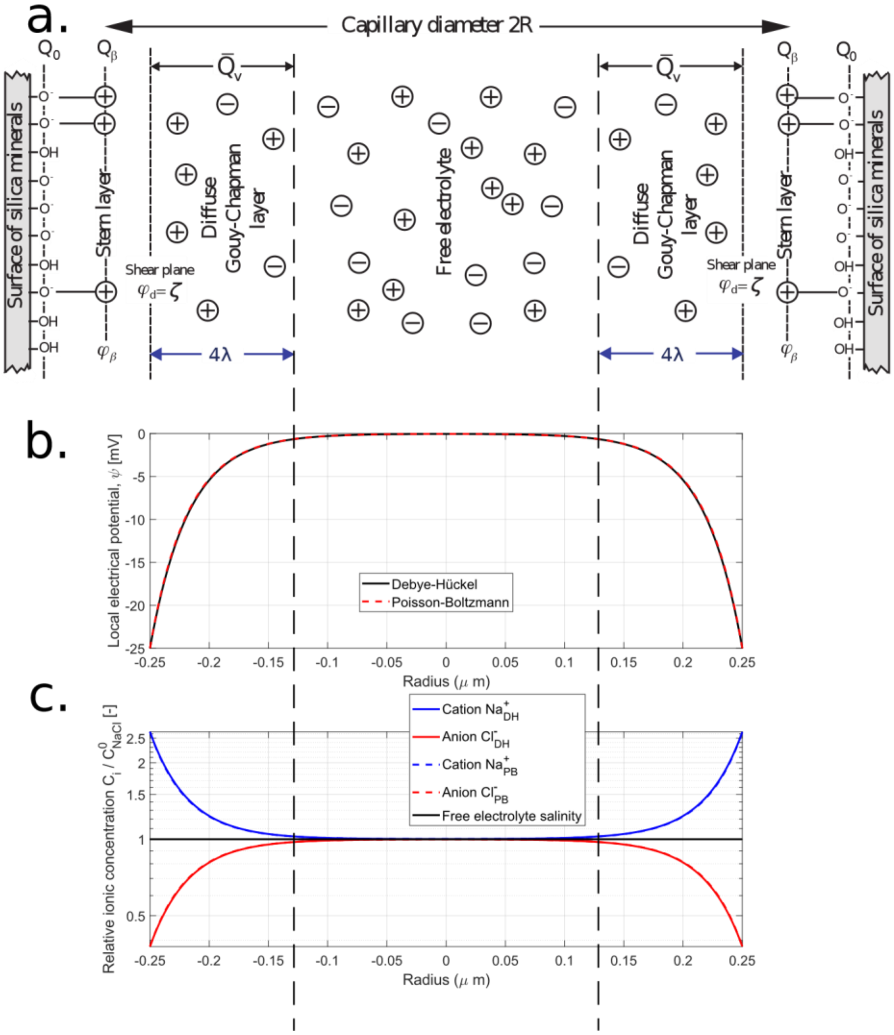

Figure 1: (a) Sketch of the electrical double layer at the surface of a mineral in contact with water. Comparison between the Debye-Hückel (DH) approximation (plain line, Eq. (13)) and the Poisson-Boltzman equation (dashed line) to compute (b) the electrical potential distribution and (c) the ionic species relative concentration distribution in a capillary (R = 0.25 μm) containing a NaCl electrolyte with 10^{-4} mol/L (i.e., λ = 0.0304 μm). Note that the dashed and plain lines are perfectly superimposed, validating the use of Eq. (13).

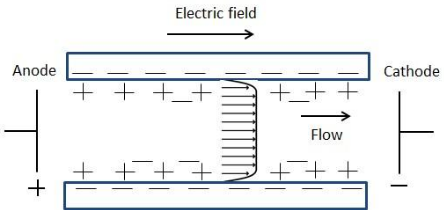

Figure 2: Electroosmosis flow in a capillary tube.

Jacob & Subirm, 2006) as shown in Fig. 1. The pore fluid nearby solid solution interface contains an excess of charges (counter-ions) to insure the electro-neutrality of the entire system. These counter-ions are often cations and surface charges are often negatively charged in environmental conditions. Note that the surface charges strongly depend on the pH and that the sign can change at low pH. The value at which the sign changes is called the point of zero charge (e.g., Hunter, 1981; Leroy & Revil, 2004). This gives rise to the charge distribution known as the electrical double layer (EDL) as shown in Fig. 1a. The EDL is composed of a Stern layer, where counter-ions are adsorbed onto the solid surface and are immobile, and a diffuse layer that contains mobile counter-ions and co-ions. In the diffuse layer, the distribution of ions and electric potential are governed by the Poisson-Boltzman (PB) equation in quasistatic conditions. The solution to the linear PB equation for a cylinder is well-known and the electric potential decays over distance from the charged surface as displayed in Fig. 1b using the code provided by Leroy & Maineult (2018). Further away from the solid-solution is the bulk electrolyte, free from surface charge influence, it contains an equal number of cations and anions and is therefore electrically neutral (Fig. 1c). The shear plane or the slipping plane is the closest place to the solid in which water flow occurs and the electrical potential at this plane is called the zeta potential (ζ). The zeta potential depends on parameters including mineral composition of porous media, ionic species that are present in the fluid, the pH of the fluid, fluid electrical conductivity and temperature etc. (see Hunter (1981); Davis et al. (1978); Jaafar et al. (2009) for more details). Reuss (1809) carried out the first experiment on electroosmosis by applying a DC voltage across a water saturated porous sample in a U-tube. When a DC voltage is applied across a capillary containing water, ions in the EDL are submitted to an electric force and move to the electrode of opposite polarity. That leads to the movement of the fluid near the solid surface as well as the bulk liquid due to viscous forces. The net motion of liquid is called electroosmotic flow (Fig. 2). The pressure necessary to counterbalance electroosmotic flow is defined as the electroosmotic pressure (e.g., Jacob & Subirm, 2006).

2.2. Governing equations

The electrokinetic coupling in a fluid saturated porous medium is described by two linear equations (e.g., Li et al., 1995; Pengra et al., 1999)

$$\mathbf{U}_e = -\sigma \nabla V - \Pi_{12} \nabla P. \tag{1}$$

$$\mathbf{U}^{f} = -\Pi_{21} \nabla V - \frac{k}{\eta} \nabla P, \tag{2}$$

where $\mathbf{U}_e$ and $\mathbf{U}_f$ are the electric current density (A m^{-2}) and Darcy flux (m s^{-1}), V is the electrical potential (V), P is the pressure that drives the flow, σ and k are the electrical conductivity (S m^{-1}) and permeability (m^2) of the porous medium, η is the dynamic viscosity of the fluid, the off-diagonal coefficients (Π_{12} and Π_{21}) are the electrokinetic coupling coefficients. In the steady state, those coupling coefficients must satisfy the reciprocal relation of Onsager: $\Pi_{12}=\Pi_{21}=\Pi$.

The streaming potential coefficient is defined when the electric current density $\mathbf{U}_e$ is zero (e.g., Li et al., 1995; Wang et al., 2016), leading to

$$K_S = \frac{\Delta V}{\Delta P} = -\frac{\Pi}{\sigma.} \tag{3}$$

Note that another formulation in which streaming potential coefficient for saturated porous media is described through the effective excess charge density $\widehat{Q}_v$ (C/m^3) dragged by the flow of the pore water was proposed by (e.g., Revil & Leroy, 2004; Revil & Linde, 2006)

$$K_S = -\frac{\widehat{Q}_v k}{\sigma \eta}\,. \tag{4}$$

The electroosmotic pressure coefficient is defined when the Darcy flux $\mathbf{U}_f$ is zero (e.g., Li et al., 1995; Wang et al., 2016), leading to

$$K_E = \frac{\Delta P}{\Delta V} = -\frac{\Pi \eta}{k}\,. \tag{5}$$

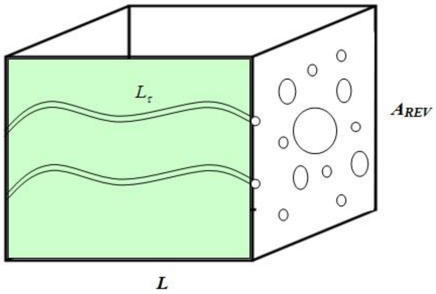

Figure 3: Sketch of the considered conceptual representative elementary volume (REV): Parallel and tortuous capillary tubes with radii following a fractal distribution.

By the volume averaging approach, Pride (1994) obtained the steady state coupling coefficient under a thin electrical double layer assumption as

$$\Pi = \frac{\phi}{\tau}\frac{\epsilon_r \epsilon_0 \zeta}{\eta} = \frac{\epsilon_r \epsilon_0 \zeta}{F\eta}\,, \tag{6}$$

where $_r$ is the relative permittivity of the fluid, $_0$ is the dielectric permittivity in vacuum, φ, τ and F are the porosity, hydraulic tortuosity and formation factor of porous media, respectively. Note that the link $\varphi F = \tau$ has been used in Eq. (6) (e.g., Wyllie & Rose, 1950; Ghanbarian et al., 2013)

Substituting Eq. (6) into Eq. (5), one obtains

$$K_E = -\frac{\epsilon_r \epsilon_0 \zeta}{Fk}\,. \tag{7}$$

In this work, we will obtain the analytical models for K_E as well as other quantities based on a fractal upscaling approach instead of the volume averaging approach for partially saturated porous media.

3. Model development

3.1. Electrical potential distribution at pore scale

Consider binary symetric 1:1 electrolytes (e.g., NaCl) of bulk ionic concentration C^0 (mol/m^3) with an electrical potential $\psi(r)$ (V) at a distance r from the axis. If the excess charge density at this point is $\rho(r)$ (C m^{-3}), then the Poisson equation is given by (e.g., Rice & Whitehead, 1965; Gierst, 1966)

$$\frac{1}{r}\frac{d}{dr}\left(r\frac{d\psi(r)}{dr}\right) = -\frac{\rho(r)}{\epsilon_r\epsilon_0}, \tag{8}$$

From the Boltzmann equation, the following is obtained

$$\rho(r) = NeC^0\left[e^{-\frac{e\psi(r)}{k_bT}} - e^{\frac{e\psi(r)}{k_bT}}\right] = 2NeC^0\sinh\frac{e\psi(r)}{k_bT} \tag{9}$$

where k_b is the Boltzmann's constant, T is temperature (in K), N is the Avogadro number and e is the elementary charge.

If $\left|\frac{e\psi(r)}{k_bT}\right| << 1$ that is called the Debye-Hückel approximation (e.g., Pride, 1994; Hunter, 1981; Jougnot et al., 2019), $\sinh\frac{e\psi(r)}{k_bT} \approx \frac{e\psi(r)}{k_bT}$. The Poisson Boltzmann equation now becomes

$$\frac{1}{r}\frac{d}{dr}\left(r\frac{d\psi(r)}{dr}\right) = -\frac{2Ne^2C^0}{\epsilon_0\epsilon_r k_bT}\psi(r) \tag{10}$$

or

$$\frac{1}{r}\frac{d}{dr}\left(r\frac{d\psi(r)}{dr}\right) = -\frac{\psi(r)}{\lambda^2} \tag{11}$$

where $\lambda = \sqrt{\frac{\epsilon_0\epsilon_r k_bT}{2Ne^2C^0}}$ is defined as the Debye length (e.g., Israelachvili, 1992). The boundary conditions of Eq. (11) to be satisfied for the cylindrical capillary surface are (Rice & Whitehead, 1965):

$$\psi(r) = \begin{cases}\psi(R) = \zeta \\ \frac{d\psi(r)}{dr}\Big|_{r=0} = 0\end{cases} \tag{12}$$

Under the boundary conditions given by Eq. (12), the analytical solution of $\psi(r)$ and $\rho(r)$ are obtained as (Rice & Whitehead, 1965)

$$\psi(r) = \zeta\frac{I_o(\frac{r}{\lambda})}{I_o(\frac{R}{\lambda})} \tag{13}$$

and

$$\rho(r) = -\frac{\epsilon_0\epsilon\zeta}{\lambda^2}\frac{I_o(\frac{r}{\lambda})}{I_o(\frac{R}{\lambda})} \tag{14}$$

where I_0 is the zero-order modified Bessel function of the first kind. Figure 1 compares the potential and concentrations of ions in the EDL calculated from Eq. (13) and the exact Poisson-Boltzmann solution (see Leroy & Maineult (2018) for more details). It shows that Eq. (13) is a correct approximation for the Poisson-Boltzmann true solution.

3.2. Velocity distribution at pore scale

Under application of an electric field E and a fluid pressure difference ΔP across a tortuous capillary of radius R, the fluid flow is the sum of a Poiseuille flow generated by ΔP and an electroosmotic flow generated by E acting on the charge density in the EDL given by Eq. (14). Consequently, the velocity profile $v(r)$ in a cylindrical capillary is given as (Rice & Whitehead, 1965)

$$v(r) = \frac{1}{4\eta}(R^2 - r^2)\frac{\Delta P}{L_\tau} + \frac{\epsilon_r\epsilon_0\zeta E}{\eta}\left[1 - \frac{I_0(r/\lambda)}{I_0(R/\lambda)}\right], \tag{15}$$

where L_τ is the length of tortuous capillaries.

Because the electric field E is related to the applied voltage across the porous medium ΔV by $E = \Delta V/L$ (L is the length of the porous medium as shown in Fig. 3). Eq. (15) is rewritten as

$$v(r) = \frac{1}{4\eta}(R^2 - r^2)\frac{\Delta P}{L_\tau} + \frac{\epsilon_r\epsilon_0\zeta}{\eta}\left[1 - \frac{I_0(r/\lambda)}{I_0(R/\lambda)}\right]\frac{\Delta V}{L}. \tag{16}$$

The volume flow rate in the capillary is

$$q(R) = \int_0^R v(r)2\pi r dr = \frac{\pi R^4}{8\eta}\frac{\Delta P}{L_\tau} + \frac{\pi\epsilon_r\epsilon_0\zeta R^2}{\eta}\left[1 - \frac{2\lambda I_1(R/\lambda)}{R I_0(R/\lambda)}\right]\frac{\Delta V}{L}, \tag{17}$$

where I_1 is the first-order modified Bessel functions of the first kind.

Figure 4 shows the variation of the nondimensional parameter of the second term in square brackets in Eq. (17) denoted by $C = 2\lambda I_1(R/\lambda)/(RI_0(R/\lambda))$ with R/λ. It is seen that when the pore size is much bigger than the Debye length (hundred times), the term of $2\lambda I_1(R/\lambda)/(RI_0(R/\lambda))$ is much smaller than the unity and can be ignored (see Rice & Whitehead (1965) for more details). Under that condition called the thin EDL assumption, Eq. (17) becomes

$$q(R) = \frac{\pi R^4 \Delta P}{8\eta L_\tau} + \frac{\pi \epsilon_r \epsilon_0 \zeta R^2}{\eta} \frac{\Delta V}{L}. \tag{18}$$

In geological media and under most environmental conditions (i.e., groundwater for human consumption or subsurface reservoirs), ionic strengths (i.e., a proxy for ionic concentration) in potable water typically vary between 10^{-3} and 10^{-2} mol/L (Jougnot et al., 2019). Reservoirs can be saturated with brine having much higher ionic concentrations depending on the formation. Therefore, the Debye length is typically less than 10 nm at 25° C (Israelachvili, 1992). It suggests that the minimum pore radius of porous materials that is applicable for thin EDL under the environmental conditions is around 100×10 nm = 1μm. In addition, typical characteristic radius of pore in geological media is tens of micrometer (e.g., Hu et al., 2017). Therefore, a thin EDL assumption (no EDL overlap) is normally satisfied in most natural systems (see Jougnot et al. (2019) for more details). It is noted that the thin EDL assumption does not work for clay rocks and low permeability sediments where the pore size is on the order of 10 nm. Therefore, one needs to take into account the term of $C = 2\lambda I_1(R/\lambda)/(RI_0(R/\lambda))$ in Eq. (17). It is therefore a limitation to the proposed model.

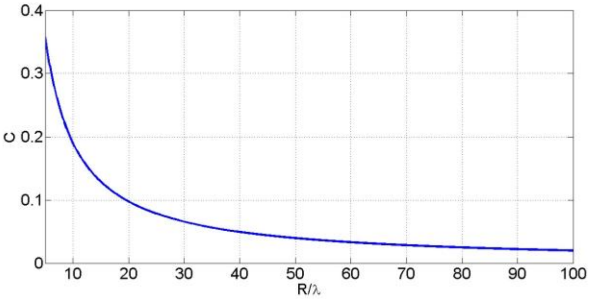

Figure 4: The variation of the unitless coefficient $C = 2\lambda I_1(R/\lambda)/(RI_0(R/\lambda))$ with the unitless ratio of the considered pore size and the Debye length (R/λ)

3.3. Fractal based up-scaling

Porous media can be conceptualized as a bundle of tortuous capillary tubes following a fractal pore-size distribution (e.g., Yu & Cheng, 2002; Liang et al., 2014) (see Fig. 3). The fractal approach is a simple and elegant way to upscale microscopic properties to macroscopic properties by assuming that the pore size distribution follows the fractal scaling law

$$N(\geq R) = (\frac{R_{max}}{R})^{D_f}, \qquad (19)$$

where *N* is the number of capillaries with radius greater than *R*, R_{max} is the maximum radius, D_f is the fractal dimension for pore space, $0 < D_f < 2$ in two-dimensional space and $0 < D_f < 3$ in three dimensional space (Yu & Cheng, 2002; Liang et al., 2014).

From Eq. (19), the following is obtained

$$-dN = D_f R_{max}^{D_f} R^{-D_f-1} dR, \qquad (20)$$

where $-dN$ is the number of capillaries with radius ranging from *R* to $R+dR$. The minus (-) in Eq. (20) implies that the number of pores decreases with the increase of pore size. The total number of capillaries with radius ranging from R_{min} (the minimum radius) to R_{max} (the maximum radius) is given by

$$N_{total}(\geq R_{min}) = (\frac{R_{max}}{R_{min}})^{D_f}. \qquad (21)$$

From Eq. (20) and Eq. (21), the following is obtained

$$-\frac{dN}{N_{total}} = D_f R_{min}^{D_f} R^{-D_f-1} dR = f(R)dR, \qquad (22)$$

in which $f(R) = D_f R_{min}^{D_f} R^{-D_f-1}$ is the probability density function. According to the statistical theory, the probability density function needs to meet the following condition

$$\int_{R_{min}}^{R_{max}} f(R)dR = 1 - (\frac{R_{min}}{R_{max}})^{D_f} = 1 \qquad (23)$$

or

$$(\frac{R_{min}}{R_{max}})^{D_f} \approx 0 \quad . \tag{24}$$

Eq. (24) is approximately valid for $R_{min}/R_{max} \approx 10^{-2}$ or $< 10^{-2}$ (Yu & Cheng, 2002; Liang et al., 2014). That condition generally holds in porous media. The fractal dimension D_f is linked to the porosity of porous media and the ratio of the minimum capillary radius to the maximum capillary radius ($\alpha = R_{min}/R_{max}$) by following equation (e.g., Yu et al., 2001; Yu & Cheng, 2002)

$$D_f = 2 - \frac{\ln\phi}{\ln\alpha} \tag{25}$$

3.4. REV scale

To obtain the volume flow rate at the macroscale, a representative elementary volume (REV) as a cube with a length *L* is considered. As presented in the previous section, the porous medium exhibits a fractal pore size distribution with radii varying from R_{min} to R_{max}. We consider the REV under varying saturation conditions. The effective saturation is defined by

$$S_e = \frac{S_w - S_{irr}}{1 - S_{irr}} \ , \tag{26}$$

where S_w is the water saturation and S_{irr} is irreducible water saturation.

We assume that the REV is initially fully saturated and then drained when submitted to a pressure head *h* (m). For a capillary tube, the pore radius R_h (m) that is drained at a given pressure head *h* can be calculated by (Jurin, 1719)

$$h = \frac{2T_s cos\beta}{\rho_w g R_h} \ , \tag{27}$$

where T_s (N/m) is the surface tension of the fluid and β is the contact angle. A capillary becomes fully desaturated under the pressure head *h* if *R* is greater than the radius R_h given by Eq. (27). Therefore, the capillaries with radii *R* between R_{min} and R_h will be fully saturated under the pressure head *h*.

For porous media containing only large and regular pores, the irreducible water saturation can often be neglected. For porous media containing small pores, the irreducible water saturation can be pretty significant because water remains trapped in the crevices or in micropores that are not occupied by air. This amount of water is taken into account in the model by setting irreducible water radius of capillaries R_{irr}. Consequently, the following assumptions are made in this work: (1) for $R_{min} \leq R \leq R_{irr}$, the capillaries are occupied by water that is immobile at irreducible saturation due to insufficient driving force, so it does not contribute to fluid flow; (2) for $R_{irr} < R \leq R_h$, the capillaries are occupied by mobile water, so it contributes to the fluid flow; (3) for $R_h < R \leq R_{max}$, the capillaries are occupied by air, so it does not contribute to the fluid flow. In this work, film bound water adhering to the capillary walls of porous media with radius greater than R_{irr} is ignored. Therefore, the irreducible water saturation is defined as

$$S_{irr} = \frac{\int_{R_{min}}^{R_{irr}} \pi R^2 L_\tau (-dN)}{\int_{R_{min}}^{R_{max}} \pi R^2 L_\tau (-dN)} = \frac{R_{irr}^{2-D_f} - R_{min}^{2-D_f}}{R_{max}^{2-D_f} - R_{min}^{2-D_f}}. \tag{28}$$

The water saturation is determined as:

$$S_w = \frac{\int_{R_{min}}^{R_h} \pi R^2 L_\tau (-dN)}{\int_{R_{min}}^{R_{max}} \pi R^2 L_\tau (-dN)} = \frac{R_h^{2-D_f} - R_{min}^{2-D_f}}{R_{max}^{2-D_f} - R_{min}^{2-D_f}}. \tag{29}$$

Because only capillaries with radius between R_{min} and R_h are fully saturated under a pressure head h, the volumetric flow rate Q_{REV} through the REV is the sum of the flow rates over all capillaries with radius between R_{irr} and R_h and given by

$$Q_{REV} = \int_{R_{irr}}^{R_h} q(R)(-dN) \tag{30}$$

Combining Eq. (18), Eq. (20) and Eq. (30), the following is obtained

$$Q_{REV} = \frac{\pi R_{max}^{D_f}}{8\eta} \frac{D_f (R_h^{4-D_f} - R_{irr}^{4-D_f})}{(4 - D_f)} \frac{\Delta P}{L_\tau} + \frac{\pi R_{max}^{D_f} \epsilon_r \epsilon_0 \zeta}{\eta} \frac{D_f (R_h^{2-D_f} - R_{irr}^{2-D_f})}{(2 - D_f)} \frac{\Delta V}{L} \tag{31}$$

Additionally, from Eq. (28) and Eq. (29) one has

$$R_{irr} = R_{max} \left[\alpha^{2-D_f} + S_{irr}(1 - \alpha^{2-D_f}) \right]^{\frac{1}{2-D_f}} \tag{32}$$

and

$$R_h = R_{max}\left[\alpha^{2-D_f} + S_w(1-\alpha^{2-D_f})\right]^{\frac{1}{2-D_f}}, \quad (33)$$

where $\alpha = R_{min}/R_{max}$.

Combining Eq. (31), Eq. (32) and Eq. (33), the following is obtained

$$\begin{aligned} Q_{REV} =& \frac{\pi R_{max}^4 D_f}{8\eta(4-D_f)}\left\{\left[\alpha^{2-D_f} + S_w(1-\alpha^{2-D_f})\right]^{\frac{4-D_f}{2-D_f}} - \left[\alpha^{2-D_f} + S_{irr}(1-\alpha^{2-D_f})\right]^{\frac{4-D_f}{2-D_f}}\right\}\frac{\Delta P}{L_\tau} \\ &+ \frac{\pi R_{max}^2 \epsilon_r \epsilon_0 \zeta D_f}{\eta(2-D_f)} S_w(1-\alpha^{2-D_f})(S_w - S_{irr})\frac{\Delta V}{L}. \end{aligned} \quad (34)$$

The total flow rate Q through the porous medium is given by

$$Q = Q_{REV}\frac{A}{A_{REV}}, \quad (35)$$

where A and A_{REV} are the cross sectional areas of the porous medium and the REV, both are perpendicular to the flow direction.

The porosity is calculated by

$$\phi = \frac{V_{pore}}{V_{REV}} = \frac{\int_{R_{min}}^{R_{max}} L_\tau \pi R^2(-dN)}{L A_{REV}} = \frac{\pi\tau D_f R_{max}^2(1-\alpha^{2-D_f})}{(2-D_f)A_{REV}}, \quad (36)$$

where τ is the mean tortuosity of the porous medium defined by the relation $L_\tau = \tau.L$.

The cross sectional area of the REV is therefore obtained as

$$A_{REV} = \frac{\pi\tau D_f R_{max}^2(1-\alpha^{2-D_f})}{(2-D_f)\phi}. \quad (37)$$

Combining Eq. (34), Eq. (35) and Eq. (37), one obtains

$$\begin{aligned} Q =& \frac{R_{max}^2 A}{8\eta\tau}\frac{(2-D_f)}{(4-D_f)}\frac{\phi}{(1-\alpha^{2-D_f})}\times \\ &\left\{\left[\alpha^{2-D_f} + S_w(1-\alpha^{2-D_f})\right]^{\frac{4-D_f}{2-D_f}} - \left[\alpha^{2-D_f} + S_{irr}(1-\alpha^{2-D_f})\right]^{\frac{4-D_f}{2-D_f}}\right\}\frac{\Delta P}{L_\tau} \\ &+ \frac{\epsilon_r\epsilon_0\zeta\phi A}{\eta\tau}(S_w - S_{irr})\frac{\Delta V}{L} \end{aligned} \quad (38)$$

Eq. (38) indicates that the total volumetric flow rate relates to the zeta potential, fluid properties (relative permittivity, viscosity), water saturation, irreducible water saturation as well as the microstructural parameters of porous media (D_f, φ, α, r_{max},τ). Eq. (38) predicts that when $S_w = S_{irr}$ (S_e=0) then $Q = 0$ (i.e., no water flow). When the porous medium is fully saturated $S_w = 1$ and the irreducible water saturation equals zero $S_{irr} = 0$, the total volumetric flow Q becomes

$$Q = \frac{R_{max}^2 A}{8\eta\tau}\frac{(2-D_f)}{(4-D_f)}\frac{\phi}{(1-\alpha^{2-D_f})}(1-\alpha^{4-D_f})\frac{\Delta P}{L_\tau} + \frac{\epsilon_r\epsilon_0\zeta\phi A}{\eta\tau}\frac{\Delta V}{L} \tag{39}$$

Because $1 < D_f < 2$ and $2 < 4 - D_f < 3$, $\alpha^{4-D_f} << 1$ ($\alpha = R_{min}/R_{max} \leq 10^{-2}$ in porous media as previously reported). Using $1 - \alpha^{2-D_f} = 1 - \varphi$ as shown by Eq. (25), Eq. (39) is rewritten as

$$Q = \frac{R_{max}^2 A}{8\eta\tau}\frac{(2-D_f)}{(4-D_f)}\frac{\phi}{(1-\phi)}\frac{\Delta P}{L_\tau} + \frac{\epsilon_r\epsilon_0\zeta\phi A}{\eta\tau}\frac{\Delta V}{L} \tag{40}$$

Eq. (40) is exactly the same as that reported in Liang et al. (2015) under the thin EDL assumption and full saturation.

From Eq. (38), we will obtain the link between fluid pressure difference and flow rate as well as the electroosmotic pressure coefficient.

3.5. Relationship between the flow rate and back pressure difference

Under the condition of zero flow rate (Q = 0), the maximum ΔP_m back pressure generated across the porous medium is obtained as

$$\Delta P_m = -\frac{8\epsilon_r\epsilon_0\zeta\Delta V\tau(1-\phi)(4-D_f)}{R_{max}^2(2-D_f)} \times \frac{S_w - S_{irr}}{\left\{[\alpha^{2-D_f} + S_w(1-\alpha^{2-D_f})]^{\frac{4-D_f}{2-D_f}} - [\alpha^{2-D_f} + S_{irr}(1-\alpha^{2-D_f})]^{\frac{4-D_f}{2-D_f}}\right\}}. \tag{41}$$

Under the condition of zero back pressure difference (ΔP = 0), the total flow rate is maximum as

$$Q_m = \frac{\epsilon_r\epsilon_0\zeta A\phi}{\eta\tau}(S_w - S_{irr})\frac{\Delta V}{L} \tag{42}$$

Combining Eq. (38), Eq. (41) and Eq. (42), the link between the pressure difference and the flow rate is given by

$$Q = Q_m \left[1 - \frac{\Delta P}{\Delta P_m}\right] \tag{43}$$

Eq. (43) is exactly the same as that obtained in Zeng et al. (2001) in which the porous medium was conceptualized as a bundle of parallel capillaries of the same radii at full saturation condition. Interestingly, Eq. (43) is obtained in this work for the fractal pore size distribution and for partially saturated porous media but the result is the same for the relationship between flow rate and pressure difference.

3.6. Electroosmotic pressure coefficient

The electroosmotic pressure coefficient K_E is defined by $\Delta P/\Delta V$, that means the K_E is a macroscopic variable (i.e., integrating over the entire bundle of capillaries) when the total flow rate Q in Eq. (38) equals zero (Li et al., 1995; Wang et al., 2016). Consequently, one has

$$K_E = \frac{\Delta P}{\Delta V}|_{Q=0} = \frac{\Delta P_m}{\Delta V} \tag{44}$$

Using Eq. (41), Eq. (44) is rewritten as

$$K_E = -\frac{8\epsilon_r\epsilon_0\zeta\tau(1-\phi)(4-D_f)}{R_{max}^2(2-D_f)} \times \frac{S_w - S_{irr}}{\left\{[\alpha^{2-D_f} + S_w(1-\alpha^{2-D_f})]^{\frac{4-D_f}{2-D_f}} - [\alpha^{2-D_f} + S_{irr}(1-\alpha^{2-D_f})]^{\frac{4-D_f}{2-D_f}}\right\}}. \tag{45}$$

Eq. (45) is a general expression for the electroosmotic pressure coefficient for partially saturated porous media. Eq. (45) indicates that the electroosmotic pressure coefficient is explicitly linked to ζ, microstructural parameters of porous media (D_f, φ, α, R_{max}, τ), water saturation and irreducible water saturation. Therefore, the model can indicate more mechanisms influencing the electroosmotic pressure coefficient than other published models (e.g., Eq. (7) deduced by the volume averaging approach).

In case of full saturation $S_w = 1$, Eq. (45) becomes

$$K_E^{sat} = -\frac{8\epsilon_r\epsilon_0\zeta\tau(1-\phi)(4-D_f)}{R_{max}^2(2-D_f)}\frac{1-S_{irr}}{\left\{1-\left[\alpha^{2-D_f}+S_{irr}(1-\alpha^{2-D_f})\right]^{\frac{4-D_f}{2-D_f}}\right\}}. \tag{46}$$

The relative electroosmotic pressure coefficient K_E^r is defined as

$$\begin{aligned} K_E^r = \frac{K_E}{K_E^{sat}} &= \frac{S_w - S_{irr}}{1-S_{irr}}\frac{\left\{1-\left[\alpha^{2-D_f}+S_{irr}(1-\alpha^{2-D_f})\right]^{\frac{4-D_f}{2-D_f}}\right\}}{\left\{\left[\alpha^{2-D_f}+S_w(1-\alpha^{2-D_f})\right]^{\frac{4-D_f}{2-D_f}}-\left[\alpha^{2-D_f}+S_{irr}(1-\alpha^{2-D_f})\right]^{\frac{4-D_f}{2-D_f}}\right\}} \\ &= S_e\frac{\left\{1-\left[\alpha^{2-D_f}+S_{irr}(1-\alpha^{2-D_f})\right]^{\frac{4-D_f}{2-D_f}}\right\}}{\left\{\left[\alpha^{2-D_f}+S_w(1-\alpha^{2-D_f})\right]^{\frac{4-D_f}{2-D_f}}-\left[\alpha^{2-D_f}+S_{irr}(1-\alpha^{2-D_f})\right]^{\frac{4-D_f}{2-D_f}}\right\}}. \end{aligned} \tag{47}$$

4. Results and discussion

4.1. Predictions of the model under partially saturated conditions

The values of α between 0.001 and 0.01 are used in this section for modeling because those values are normally used in published works (Yu & Cheng, 2002; Liang et al., 2014; Thanh et al., 2019). The fractal dimension D_f is in the range between 1 and 2. For given porous media, D_f is determined via Eq. (25) with known values of α and porosity φ. Fig. 5 shows (a) the influence of the irreducible saturation on the change of the relative electroosmotic pressure coefficient K_E^r with the water saturation S_w (S_{irr} = 0.02, 0.05 and 0.1) for α = 0.01 and D_f = 1.8; (b) influence of α on the variation of K_E^r with S_w (α = 0.002, 0.005, 0.01) for S_{irr} = 0.05 and D_f = 1.8 and (c) Influence of D_f on the variation of K_E^r with S_w (D_f = 1.3, 1.5, 1.8) for α = 0.01 and S_{irr} = 0.05. The results show that as the media desaturate, the relative electroosmotic pressure coefficient K_E^r increases. The reason is that at lower water saturation, only capillaries with smaller radii are occupied by water. Therefore, one needs larger pressure differences over porous media to counterbalance with the flow rate generated by the same applied voltage (such that the total volumetric flow rate is zero). As a result, K_E^r is larger for lower water saturation. Additionally, Fig. 5 shows that the relative electroosmotic pressure coefficient is very sensitive to the fractal dimension D_f and the ratio α. It is noted that the D_f decreases with an increase of α at a given porosity as indicated by Eq. (25). Fig. 5 also shows that the K_E^r decreases with the increase of the ratio α and decrease of D_f. That can be explained by the decrease of the total number of pores in the REV with the decrease of D_f.

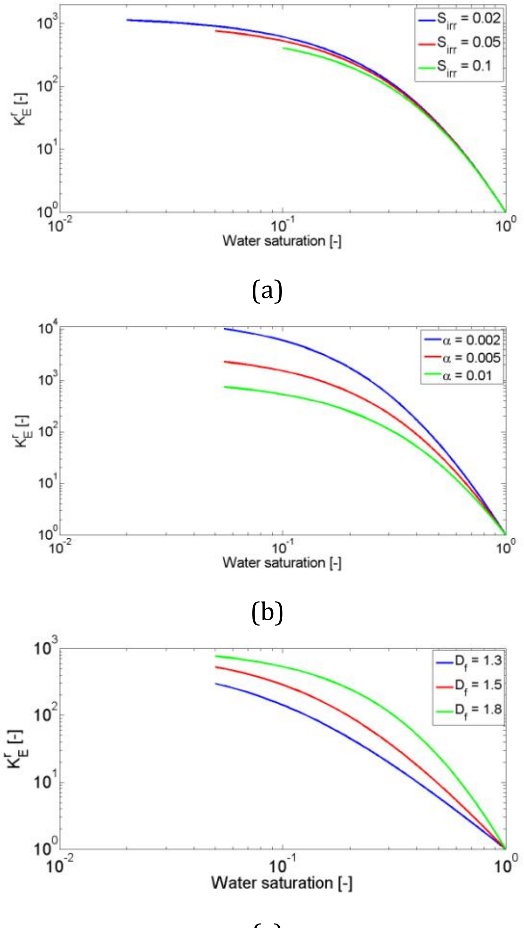

(a)

(b)

(c)

Figure 5: Sensitivity analysis of the model: (a) Influence of the irreducible saturation on the variation of the K_E^r with the water saturation S_w (S_{irr} = 0.02, 0.05 and 0.1) for α = 0.01 and D_f = 1.8; (b) Influence of α on the variation of K_E^r with S_w (α = 0.002, 0.005, 0.01) for S_{irr} = 0.05 and D_f = 1.8; (c) Influence of D_f on the variation of K_E^r with S_w (D_f = 1.3, 1.5, 1.8) for α = 0.01 and S_{irr} = 0.05.

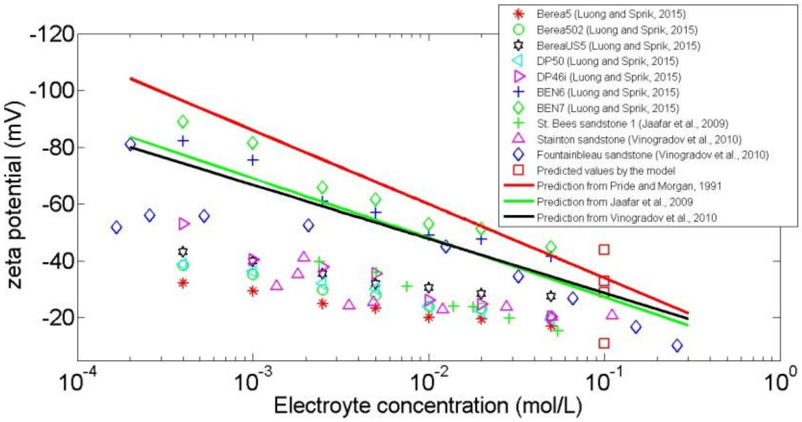

Figure 6: The variation of the zeta potential with pore fluid salinity. The predicted values of the zeta potential for four samples of glass beads at 0.1 mol/L in Li et al. (1995) are shown by red squares. Experimental data from different sources reported by Thanh & Sprik (2015),Jaafar et al. (2009) and Vinogradov et al. (2010) are also presented.

Therefore, R_h becomes larger at the same water water saturation. Similarly, we need to apply a smaller pressure difference over the partially saturated REV to counter balance the flow rate generated by the same applied voltage. Consequently, K_E^r decreases with a decrease of D_f.

4.2. Comparison with experimental data in water saturated porous media

Even if the present model is developed based on the concept of capillary tubes, it possible to provide a relationship between capillary radius to grain size for the sake of medium characterization. Indeed, in non-consolidated granular materials, pore size are very difficult to obtain without perturbating the medium, while grain sizes and grain size distribution can be easily measured. Therefore, with the knowledge of the mean grain diameter d of a granular material, the maximum pore radius can be determined by (e.g., Liang et al., 2015)

$$R_{max} = \frac{d}{4}\left[\sqrt{\frac{\phi}{1-\phi}} + \sqrt{\frac{1}{1-\phi}}\right]. \tag{48}$$

Mean geometrical tortuosity of porous media is predicted from porosity as (e.g., Cai et al., 2012a; Ghanbarian et al., 2013; Liang et al., 2015)

$$\tau = \frac{1}{2}\left[1 + \frac{1}{2}\sqrt{1-\phi} + \sqrt{1-\phi}\frac{\sqrt{(1/\sqrt{1-\phi}-1)^2 + 1/4}}{1-\sqrt{1-\phi}}\right] \tag{49}$$

Table 1: Input parameters of four samples of fused glass beads are taken from Li et al. (1995). Symbols of d, φ, K_E and α are symbols for the grain diameter, porosity, the electroosmotic pressure coefficient and ratio of minimum and maximum radius, respectively. The values of ζ are predicted from Eq. (45)

Number	d (μm)	φ (no units)	K_E (Pa/V)	α (no units)	ζ (mV)
1	50	0.10	4.94	0.01	-11
2	50	0.17	12.5	0.01	-48
3	100	0.19	1.9	0.01	-33
4	200	0.30	0.25	0.01	-29
mean					-30

We want to see if the model is able to predict the zeta potential using Eq. (46). Li et al. (1995) measured K_E for fused glass beads fully saturated by a 0.1 M NaCl electrolyte. Micro-structure parameters of the samples such as grain diameter d, porosity φ as well as the measured K_E are reported in Li et al. (1995) and re-shown in Table 1. At this electrolyte concentration, the Debye length λ is around 1 nm (Israelachvili, 1992). Of all samples, the minimum value of R_{max} corresponding to the sample 1 (d=50 μm and φ=0.1) is predicted using Eq. (48) to be 17 μm. Hence, R_{min} corresponding to the sample 1 is obtained using $R_{min} = \alpha R_{max} = 0.01 R_{max}$=170 nm. Consequently, the Debye length is much smaller than R_{min} and Eq. (46) is applicable for experimental data reported by Li et al. (1995).

The value of α is taken as 0.01 because that is a normally used value for grain materials (e.g., Thanh et al., 2018, 2019). The value of S_{irr} is reasonably taken as 0 for large grain materials (e.g., Jougnot et al., 2012). From the known values of porosity φ and α of samples (see Table 1), D_f is obtained by Eq. (25). From Eq. (46), the zeta potential is obtained with the knowledge of α, D_f, τ, φ, R_{max} and S_{irr}. The predicted values are presented in Table 1. It is seen that the predicted values (see red squares at 0.1 mol/L in Fig. 6) are in good agreement with published experimental data (Jaafar et al., 2009; Vinogradov et al., 2010; Thanh & Sprik, 2015).

The zeta potential is dependent on the electrical conductivity of the fluid. The electroosmotic pressure coefficient K_E^{sat} varies with the electrolyte electrical conductivity σ_w. Fig. 7 shows the variation of the electroosmotic pressure coefficient with fluid electrical conductivity experimentally obtained by

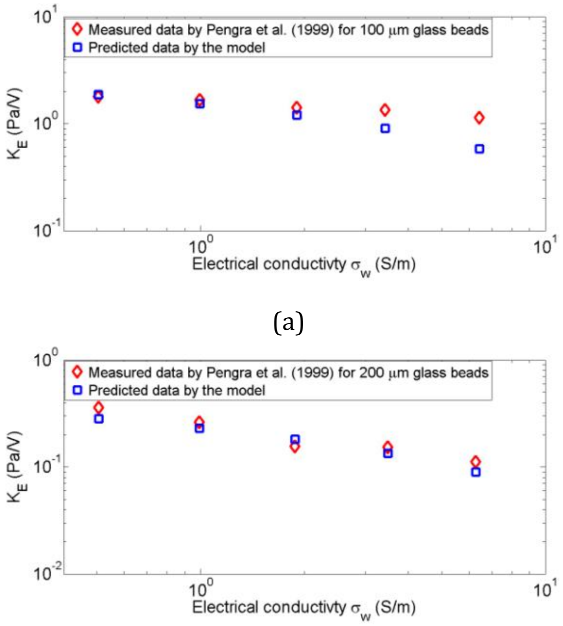

(a)

(b)

Figure 7: Variation of the electroosmotic pressure coefficient K_E^{sat} at saturated condition with electrolyte electrical conductivity for two consolidated samples of glass beads: (a) for the sample of 100 μm glass beads and (b) for the sample of 200 μm glass beads shown in Table 1).

Pengra et al. (1999) for two samples of glass beads (d=100 μm and 200 μm, respectively) saturated by a NaCl electrolyte (see diamond symbols). There are few proposed expressions for the relationship between the zeta potential and electrolyte concentration available in the literature (e.g., Pride & Morgan, 1991; Jaafar et al., 2009; Vinogradov et al., 2010). One is given by $\zeta = a + b\log10(C_f)$ with a = -6.43 mV, b = 20.85 mV as shown by Jaafar et al. (2009), for example. Electrical conductivity of the NaCl electrolyte is linked to the electrolyte concentration by the relation $\sigma_w = 10C_f$ for the ranges 10^{-6}M $< C_f <$ 1 M and 15^{o}C $< T <$ 25^{o}C (Sen & Goode, 1992). Therefore, the relation $\zeta = -6.43 + 20.85\log10(0.1\sigma_w)$ (mV) is obtained. Similarly, we obtain R_{min} = 400 nm for two samples and maximum value of λ=1.36 nm for the considered range of electrolyte concentration by Pengra et al. (1999) (from 0.05 mol/L to 0.65 mol/L). Therefore, the thin EDL assumption is satisfied. Applying the same approach as we did previously, the variation of the electroosmotic pressure coefficient K_E^{sat} with electrical conductivity σ_w is predicted as shown in Fig. 7 by square symbols. One can see that the model prediction is also in good match with data measured by Pengra et al. (1999) (diamond symbols) even there is a large difference between the model prediction and measured data for smaller glass beads at high electrical conductivity. The reason may be that Jaafar et al. (2009) obtained:

$$\zeta = a + b\log10(C_f) \tag{50}$$

by fitting experimental data for quartz, silica, glass and St. Bees in NaCl brine with big data scattering. As shown in Fig. 3 of Jaafar et al. (2009), the difference in ζ can reach 65% at $C_f = 10^{-2}$ mol/L. Therefore, the $\zeta - C_f$ relation may not work well for a single silica-based sample in a large range of electrolyte concentration. As a matter of fact, Cherubini et al. (2018) show that, for data on carbonate materials, the best fit they obtain is rather a = -6.97 mV and b = 9.13 mV, indicating that this relationship is largely mineral dependent.

Figure 8 shows the variation of ΔP_m with an applied voltage for the 10 μm sand pack saturated with 10^{-3} M NaCl. The symbols are deduced from Luong & Sprik (2013) (their Fig. 10) using the relation $\Delta P_m = \rho g \Delta h_m$ (Δh_m is the maximum height difference obtained from Luong & Sprik (2013), ρ = 1000 kg/m^3 is the water density and g =10 m/s^2 is the acceleration due to

Table 2: Parameters taken from Wang et al. (2015) for 10 sandstone samples in which φ, k, ζ stand for porosity, permeability, the zeta potential. The electroosmotic pressure coefficient K_E^{exp} is deduced by comparison between the similarity of porosity, permeability, depth of samples between Wang et al. (2015) and Wang et al. (2016). K_E^{theo} is predicted from the model.

Sample	φ (no units)	k (10^{-15} m^2)	ζ (V)	K_E^{exp} (Pa/V)	K_E^{theo} (Pa/V)
D1	30.6	1028	-0.0486	0.42	0.44
D2	30.2	1435	-0.0571	0.47	0.35
D3	30.9	1307	-0.0410	0.40	0.31
D4	32.1	1152	-0.0609	0.40	0.61
D5	29.8	456	-0.0727	0.52	1.30
D6	31.0	978	-0.0462	0.51	0.46
D7	29.4	594	-0.0627	0.49	0.82
D8	31.0	2785	-0.1448	0.52	0.51
D9	29.3	1491	-0.0765	0.43	0.40

D10	31.5	3241	-0.0639	0.51	0.21

gravity). At the saturated condition, Eq. (41) becomes

$$\Delta P_m = -\frac{8\epsilon_r\epsilon_0\zeta\Delta V\tau(1-\phi)(4-D_f)}{R_{max}^2(2-D_f)}\times \frac{1-S_{irr}}{\left\{1-\left[\alpha^{2-D_f}+S_{irr}(1-\alpha^{2-D_f})\right]^{\frac{4-D_f}{2-D_f}}\right\}} \qquad (51)$$

The solid line is predicted from Eq. (51) in the same manner as mentioned above with *φ* = 0.38, D_f= 0.01, *d* = 10 µm, *α* = 0.01 and the mean value of *ζ*= -13 mV over six granular samples made of spherical grains (Luong & Sprik, 2013) (best fit is obtained with S_{irr} = 0). Note that the thin EDL is not really met in this case because of R_{min} ≈ 60 nm and *λ* = 9.6nm. Therefore, the model may not work really well to reproduce the experimental data as shown in Fig. 8.

Eq. (46) is applied to determine the electroosmotic pressure K_E coefficient for ten sandstone samples (20 mm in length and 25 mm in diameter) saturated by a 0.05 M NaCl electrolyte reported in Wang et al. (2015). Parameters of the sandstone samples and the measured zeta potential are presented

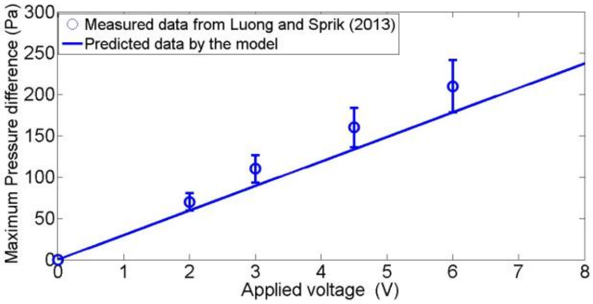

Figure 8: Maximum pressure difference as a function of applied voltage. The symbols are experimental data from Luong & Sprik (2013) with ± 15 % of uncertainty and the solid line is obtained from Eq. (51)

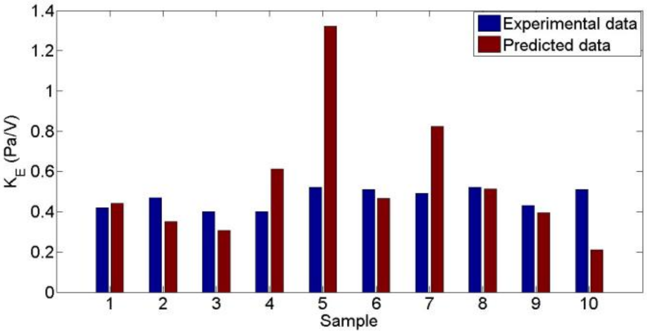

Figure 9: The variation of the K_E predicted in this work and the experimental data taken from Wang et al. (2015)

by Wang et al. (2015) and re-shown in Table 2. The measured values of K_E are obtained by the same research group Wang et al. (2016) for the same conditions and re-presented in Table 2 (see K_E^{exp}). To estimate the mean grain diameter of porous media from the permeability, we use the relation given by (e.g., Bernabe & Revil, 1995; Revil et al., 1999; Glover et al., 2006)

$$d = \sqrt{\frac{4am^2k}{\phi^{3m}}} \tag{52}$$

where the cementation exponent m is taken as 1.9 for consolidated sandstone (Friedman, 2005) and a is a constant between 2-12 that depends on the pore space (Glover et al., 2006; Glover & Walker, 2009). In this part, a is taken as 4 for a set of samples of Wang et al. (2015). With estimated values of d, measured φ and α = 0.001 (that value is also relevant to that used in Liang et al. (2014) for a Fontainebleau sandstone), the K_E is predicted for reported in Table 2 (K_E^{theo}). Fig. 9 shows the predicted K_E calculated in this work and measured values taken from Wang et al. (2015). It is seen that Eq. (46) predicts the published experimental data well. Note that for this set of experimental data, we obtain the minimum value of $R_{min} \approx 2.10^3$ nm and λ = 1.36 nm. Therefore, the thin EDL assumption is satisfied and Eq. (46) is valid.

4.3. Prediction of the product of the permeability and formation factor

Comparing Eq. (7) and Eq. (46), the product of the permeability and formation factor of porous media is given by

$$kF = \frac{R_{max}^2(2-D_f)}{8\tau(1-\phi)(4-D_f)} \frac{\left\{1-\left[\alpha^{2-D_f}+S_{irr}(1-\alpha^{2-D_f})\right]^{\frac{4-D_f}{2-D_f}}\right\}}{1-S_{irr}} \quad (53)$$

Eq. (53) indicates that based on the fractal model for electroosmostic flow in porous media, one can get the product of the permeability and formation factor from the parameters D_f, R_{max}, τ, α and S_{irr} of porous media. Eq. (53) is now used to estimate the product of kF and compare with experimental data reported in Glover et al. (2006), Glover & D´ery (2010) and Bol`eve et al. (2007) for 27 samples of bead packs. Parameters for the samples (grain diameter, porosity, permeability) are taken from Glover et al. (2006), Glover & D´ery (2010) and Bol`eve et al. (2007) and re-shown in Table 3. The values

Table 3: Input parameters for bead packs taken from Glover et al. (2006), Glover & D´ery (2010) and Bol`eve et al. (2007). Symbols of d (μm), φ (no units), k (m^2), F (no units) and α (no units) stand for grain diameter, porosity, permeability, formation factor and ratio of minimum and maximum radius, respectively.

No.	d (μm)	φ (-)	k (10^{-12} m^2)	F (-)	α (-)	reference
1	20	0.40	0.2411	3.90	0.01	Glover et al. (2006)
2	45	0.39	1.599	4.01	0.01	Glover et al. (2006)
3	106	0.39	8.118	4.04	0.01	Glover et al. (2006)
4	250	0.40	50.46	3.97	0.01	Glover et al. (2006)
5	500	0.38	186.79	4.08	0.01	Glover et al. (2006)
6	1000	0.40	709.85	3.91	0.01	Glover et al. (2006)
7	2000	0.39	2277.26	4.13	0.01	Glover et al. (2006)
8	3350	0.40	7706.97	3.93	0.01	Glover et al. (2006)
9	1.05	0.411	0.00057	3.80	0.01	Glover & D´ery (2010)
10	2.11	0.398	0.00345	3.98	0.01	Glover & D´ery (2010)
11	5.01	0.380	0.0181	4.27	0.01	Glover & D´ery (2010)
12	11.2	0.401	0.0361	3.94	0.01	Glover & D´ery (2010)
13	21.5	0.383	0.228	4.22	0.01	Glover & D´ery (2010)
14	31	0.392	0.895	4.07	0.01	Glover & D´ery (2010)
15	47.5	0.403	1.258	3.91	0.01	Glover & D´ery (2010)
16	104	0.394	6.028	4.04	0.01	Glover & D´ery (2010)
17	181	0.396	21.53	4.01	0.01	Glover & D´ery (2010)
18	252	0.414	40.19	3.75	0.01	Glover & D´ery (2010)
19	494	0.379	224	4.29	0.01	Glover & D´ery (2010)
20	990	0.385	866.7	4.19	0.01	Glover & D´ery (2010)

21	56	0.4	2.0	3.3	0.01	Bol`eve et al. (2007)
22	72	0.4	3.1	3.2	0.01	Bol`eve et al. (2007)
23	93	0.4	4.4	3.4	0.01	Bol`eve et al. (2007)
24	181	0.4	27	3.3	0.01	Bol`eve et al. (2007)
25	256	0.4	56	3.4	0.01	Bol`eve et al. (2007)
26	512	0.4	120	3.4	0.01	Bol`eve et al. (2007)
27	3000	0.4	14000	3.6	0.01	Bol`eve et al. (2007)

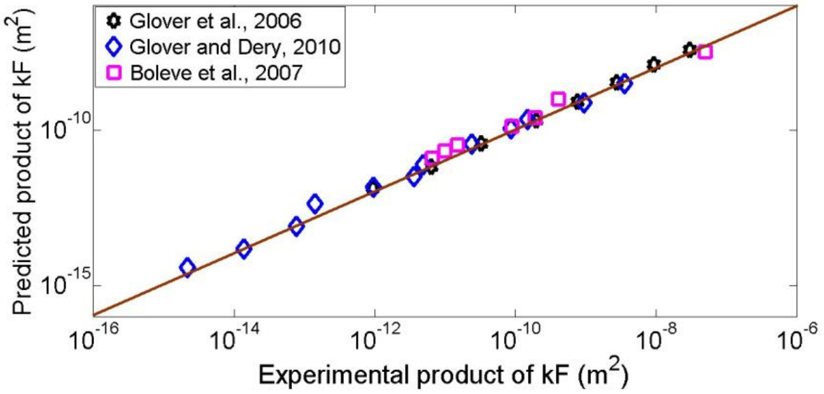

Figure 10: A comparison between *kF* predicted from Eq. (53) and from measured data in Glover et al. (2006), Glover & D´ery (2010) and Bol`eve et al. (2007) (the solid line is a 1:1 line).

of α and S_{irr} are taken as 0.01 and 0, respectively. Value of τ is obtained by the relation $\tau = \varphi F$. From those parameters in combination with Eq. (53), the product of the permeability and formation factor is predicted in the same procedure as previously mentioned. Fig. 10 shows the comparison between the product of *kF* predicted in this work and the experimental data. The solid line represents a 1:1 line. It is seen that the predicted values are in very good match with the experimental data. It suggests that one can predict *k* of porous materials from Eq. (53) with the knowledge of *F* and vice versa.

4.4. Electrokinetic coupling under partially saturated condition

Based on Eq. (3) and Eq. (5), the relationship between the electroosmosis coefficient and the streaming potential coefficient is obtained as

$$K_S(S_w) = \frac{K_E(S_w)k(S_w)}{\sigma(S_w)\eta} . \tag{54}$$

Therefore, the relative streaming potential coefficient is given as

$$K_S^r = \frac{K_S(S_w)}{K_S^{sat}(S_w=1)} = \frac{K_E(S_w)}{K_E^{sat}(S_w=1)} \frac{k(S_w)}{k(S_w=1)} \frac{\sigma(S_w=1)}{\sigma(S_w)}, \tag{55}$$

where $K_E^r = \frac{K_E(S_w)}{K_E^{sat}(S_w=1)}$ is given in Eq. (47), $\frac{k(S_w)}{k(S_w=1)}$ and $\frac{\sigma(S_w)}{\sigma(S_w=1)}$ are called the relative permeability and the relative conductivity of porous media and denoted by k^r and σ^r, respectively. In this work, we do not have expressions for k^r and σ^r based on the fractal theory yet. Therefore, we use expressions given by (e.g., Revil et al., 2007; Linde et al., 2006) for k^r and σ^r:

$$k^r = S_e^{(2+3\lambda)/\lambda} \tag{56}$$

and

$$\sigma^r = S_w^n, \tag{57}$$

where is λ is the curve-shape parameter and n is the saturation exponent. Eq. (57) is valid for the negligible surface conductivity.

Combining Eq. (47), Eq. (55), Eq. (56) and Eq. (57), the relative streaming potential coefficient is given by

$$K_S^r = S_e \frac{\left\{1 - \left[\alpha^{2-D_f} + S_{irr}(1-\alpha^{2-D_f})\right]^{\frac{4-D_f}{2-D_f}}\right\}}{\left\{\left[\alpha^{2-D_f} + S_w(1-\alpha^{2-D_f})\right]^{\frac{4-D_f}{2-D_f}} - \left[\alpha^{2-D_f} + S_{irr}(1-\alpha^{2-D_f})\right]^{\frac{4-D_f}{2-D_f}}\right\}} \times S_e^{(2+3\lambda)/\lambda} \frac{1}{S_w^n}. \tag{58}$$

Additionally, Revil et al. (2007) used the volume averaging approach to get the relative streaming potential coefficient as

$$K_S^r = S_e^{(2+3\lambda)/\lambda} \frac{1}{S_w^{n+1}}. \tag{59}$$

Figure 11 shows the change of the relative streaming potential coefficient K_S^r with the water saturation predicted from Eq. (58) and Eq. (59). Input parameters for modeling in Fig. 11 are n=2.7, λ=0.87, S_{irr}=0.36 which are reported by Revil et al. (2007), D_f=1.5 and α=0.01 which are used due to the best fit. Additionally, a comparison between those models and experimental data reported in Revil et al. (2007) for the dolomite sample E3 (square symbols) is also shown in Fig. 11. A good agreement is observed between the proposed model, the model presented by Revil et al. (2007) and experimental data. Clearly, both theoretical models are able to describe the decrease of the relative streaming potential coefficient with decreasing water saturation, from full saturation to nearly irreducible water saturation as indicated by experimental data. When S_w decreases then the number of capillaries occupied by water in the REV decreases. Hence, the streaming current through the REV generated by a fluid flow becomes smaller at a given fluid pressure difference. Consequently, the K_S^r decreases with decreasing S_w as predicted.

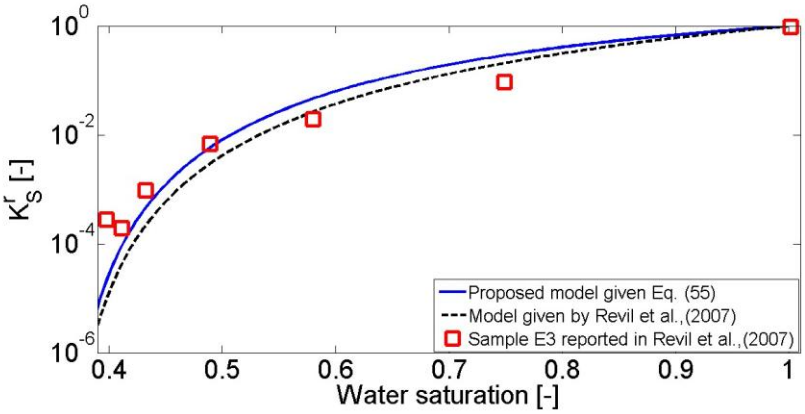

Figure 11: Variation of the coefficient K_S^r with the water saturation (n=2.7, λ=0.87, S_{irr}=0.36, D_f=1.5 and α=0.01). The solid and dashed lines correspond to the proposed model (see Eq. (58)) and the model of Revil et al. (2007), respectively.

4.5. Effective excess charge density

From Eq. (3), Eq. (4), Eq. (5) and Eq. (46), the effective excess charge density $\widehat{Q}_v$ (C/m^3) under fully saturated conditions is deduced as

$$\widehat{Q}_v = \frac{8\epsilon_r\epsilon_0\zeta\tau(1-\phi)(4-D_f)}{R_{max}^2(2-D_f)} \frac{1-S_{irr}}{\left\{1-\left[\alpha^{2-D_f}+S_{irr}(1-\alpha^{2-D_f})\right]^{\frac{4-D_f}{2-D_f}}\right\}}. \quad (60)$$

When one neglects the irreducible water saturation, Eq. (60) reduces to

$$\widehat{Q}_v = \frac{8\epsilon_r\epsilon_0\zeta\tau(1-\phi)(4-D_f)}{R^2_{max}(2-D_f)} \quad . \tag{61}$$

Based on Eq. (61), we can calculate $\widehat{Q}_v$ for the glass beads reported in Glover & D´ery (2010) and Bol`eve et al. (2007) using the same approach mentioned above. The values of the zeta potential are reported to be ζ = -24.72 mV and -73.34 mV in Glover & D´ery (2010) and ζ = -17.5 mV, -44.7

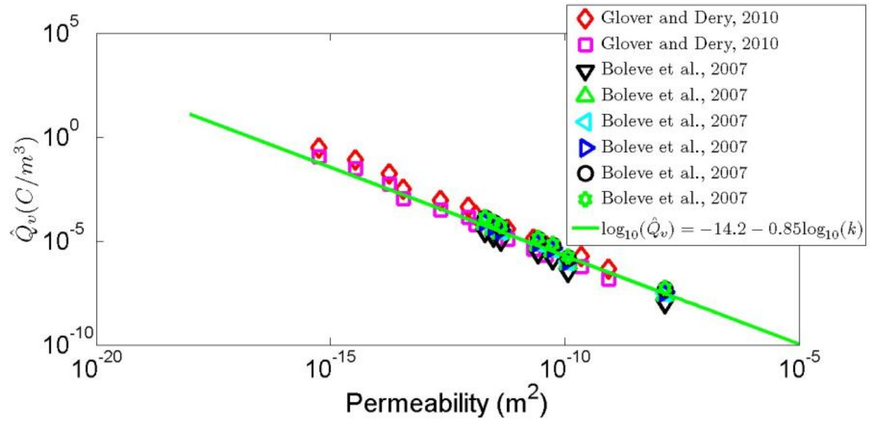

Figure 12: Variation of the effective excess charge density $Q\mathrm{b}_v$ with the permeability k. Symbols represent experimental data from Glover & D´ery (2010) and Bol`eve et al. (2007) (Table 3). The solid line is the fit line with $\log_{10}(\widehat{Q}_v)$= -14.2 -0.85$\log_{10}(k)$.

mV, -54.6 mV, -59.7 mV, -87.9 mV and -99.3 mV in Bol`eve et al. (2007) (see their Fig. 8). From calculated $\widehat{Q}_v$, we can plot the $\widehat{Q}_v - k$ graph (in which k is taken from Table 3) as shown in Fig. 12 from which we obtain the fit line: $\log_{10}(Q\mathrm{b}_v)$= A_1 +$A_2\log_{10}(k)$ with A_1 = -14.2 and A_2 = -0.85. The obtained $Q\mathrm{b}_v - k$ relationship is in good agreement with that reported by Jardani et al. (2007) by fitting to a large set of experimental data that includes various lithologies and ionic concentrations: $\log_{10}(\widehat{Q}_v)$= -9.23 -0.82 $\log_{10}(k)$. The constant A_2 = -0.85 obtained in this work is related to rock properties (R_{max}, α, τ, φ and D_f) and is very close to -0.82 reported by Jardani et al. (2007). The obtained constant A_1 = -14.2 deviates largely from value of -9.23 proposed by Jardani et al. (2007). The reason is that A_1 is mainly dependent of chemical and interface parameters (Guarracino

& Jougnot, 2018). Therefore, it varies with mineral composition of rocks, electrolyte concentration, types of electrolyte etc.

5. Conclusions

We derive a physically based model for electroosmostic flow in porous media in which the minimum pore radius is 100 times the Debye length, that is around 1 µm under environmental conditions. The porous medium is conceptualized as a bundle of tortuous capillary tubes with a pore-size distribution following a fractal law. The obtained model is linked to the applied voltage, back pressure, water saturation, irreducible water saturation and microstructural parameters of porous materials (D_f, φ, α, r_{max}, τ). From the model, the expressions for the electroosmosis pressure coefficient, the relative electroosmosis pressure coefficient, the maximum back pressure, the maximum flow rate, the flow rate-applied back pressure relation and the product of the permeability and formation factor of porous media are also obtained. To validate the model, the sensitivity of the relative electroosmosis pressure coefficient K_E^r to S_{irr}, α and D_f is analyzed and explained. The model predictions are then compared with published data in both cases of full saturation and partial saturation. The comparisons show that our model is able to explain well experimental data. From K_E^r, the expression for the relative streaming potential coefficient K_S^r is also deduced. From that, the variation of K_S^r with the water saturation is predicted and compared with another model as well as experimental data from the dolomile rock sample. Addtionally, we also obtain an expression for the effective excess charge density $\widehat{Q}_v$. We find a good agreement between those obtained expressions and published data. We believe that the model proposed in this study can open up to new studies and modelling regarding electroosmotic phenomena and paving the way to to the development of new applications and technical development in various disciplines from contaminated porous media remediation to masonery structures dewatering.

Acknowledgments

This research is funded by Vietnam National Foundation for Science and Technology Development (NAFOSTED) under grant number 103.99 2019.316. Additionally, D. Jougnot and A. Mendieta strongly thank the financial support of ANR EXCITING (grant ANR-17-CE06-0012) for the PhD thesis funding of A. Mendieta.

References

Bandopadhyay, A., DasGupta, D., Mitra, S. K., & Chakraborty, S. (2013). Electro-osmotic flows through topographically complicated porous media: Role of electropermeability tensor. *Phys. Rev. E*, *87*, 033006.

Bernabe, Y., & Revil, A. (1995). Pore-scale heterogeneity, energy dissipation and the transport properties of rocks. *Geophysical Research Letters*, *22*, 1529–1532.

Bertolini, L., Coppola, L., Gastaldi, M., & Redaelli, E. (2009). Electroosmotic transport in porous construction materials and dehumidification of masonry. *Construction and Building Materials*, *23*, 254 – 263.

Bol`eve, A., Crespy, A., Revil, A., Janod, F., & Mattiuzzo, J. L. (2007). Streaming potentials of granular media: Influence of the dukhin and reynolds numbers. *Journal of Geophysical Research*, *B08204*.

Bruell, C. J., Segall, B. A., & Walsh, M. T. (1992). Electroosomotic removal of gasoline hydrocarbons and tce from clay. *Journal of Environmental Engineering*, *118*, 68–83.

Bruus, H. (2008). *Theoretical Microfluidics*. Oxford University Press; 1 edition.

Cai, J. C., Hu, X. Y., Standnes, D. C., & You, L. J. (2012a). An analytical model for spontaneous imbibition in fractal porous media including gravity. *Colloids and Surfaces, A: Physicocemical and Engineering Aspects*, *414*, 228–233.

Cai, J. C., You, L. J., Hu, X. Y., Wang, J., & Peng, R. H. (2012b). Prediction of effective permeability in porous media based on spontaneous imbibition effect. *International Journal of Modern Physics C*, *23*, DOI: 10.1142/S0129183112500544.

Casagrande, L. (1983). Stabilization of soils by means of electroosmotic state-of-art. *Journal of Boston Society of Civil Engineering, ASCE*, *69*, 255–302.

Cherubini, A., Garcia, B., Cerepi, A., & Revil, A. (2018). Streaming potential coupling coefficient and transport properties of unsaturated carbonate rocks. *Vadose Zone Journal*, *17*, 180030.

Davis, J., James, R., & Leckie, J. (1978). Surface ionization and complexation at the oxide/water interface. i. computation of electrical double layer properties in simple electrolytes. *Journal of Colloid and Interface Science*, *63*.

Feder, J., & Aharony, A. (1989). *Fractals in Physics*. North Holland, Amsterdam.

Friedman, S. P. (2005). Soil properties influencing apparent electrical conductivity: a review. *Computers and Electronics in Agriculture*, *46*, 45 – 70.

Ghanbarian, B., Hunt, A., P. Ewing, R., & Sahimi, M. (2013). Tortuosity in porous media: A critical review. *Soil Science Society of America Journal*, *77*, 1461–1477.

Gierst, L. (1966). Double layer and electrode kinetics. *Journal of the American Chemical Society*, *88*, 4768–4768.

Glover, P., I. Zadjali, I., & A Frew, K. (2006). Permeability prediction from micp and nmr data using an electrokinetic approach. *Geophysics*, *71*, F49–F60.

Glover, P. W. J., & D´ery, N. (2010). Streaming potential coupling coefficient of quartz glass bead packs: Dependence on grain diameter, pore size, and pore throat radius. *Geophysics*, *75*, F225–F241.

Glover, P. W. J., & Walker, E. (2009). Grain-size to effective pore-size transformation derived from electrokinetic theory. *Geophysics*, *74(1)*, E17–E29.

Good, B. T., Bowman, C. N., & Davis, R. H. (2006). An effervescent reaction micropump for portable microfluidic systems. *Lab Chip*, *6*, 659–666.

Guarracino, L., & Jougnot, D. (2018). A physically based analytical model to describe effective excess charge for streaming potential generation in water saturated porous media. *Journal of Geophysical Research: Solid Earth*, *123*, 52–65.

Han, S.-J., Kim, S.-S., & Kim, B.-I. (2004). Electroosmosis and pore pressure development characteristics in lead contaminated soil during electrokinetic remediation. *Geosciences Journal*, *8*, 85.

Hu, G., & Li, D. (2007). Multiscale phenomena in microfluidics and nanofluidics. *Chemical Engineering Science*, *62*, 3443 – 3454.

Hu, X., Hu, S., Jin, F., & Huang, S. (2017). *Physics of Petroleum Reservoirs*. Springer-Verlag Berlin Heidelberg.

Hunter, R. J. (1981). *Zeta Potential in Colloid Science*. Academic, New York.

Israelachvili, J. (1992). *Intermolecular and Surface Forces*. Academic Press.

Jaafar, M. Z., Vinogradov, J., & Jackson, M. D. (2009). Measurement of streaming potential coupling coefficient in sandstones saturated with high salinity nacl brine. *Geophysical Research Letters*, *36*, doi:10.1029/2009GL040549.

Jacob, H. M., & Subirm, B. (2006). *Electrokinetic and Colloid Transport Phenomena*. Wiley-Interscience.

Jardani, A., Revil, A., Boleve, A., Crespy, A., Dupont, J.-P., Barrash, W., & Malama, B. (2007). Tomography of the darcy velocity from self-potential measurements. *Geophysical Research Letters*, *34*.

Jougnot, D., Linde, N., Revil, A., & Doussan, C. (2012). Derivation of soil-specific streaming potential electrical parameters from hydrodynamic characteristics of partially saturated soils. *Vadose Zone Journal*, *11*, 272–286.

Jougnot, D., Mendieta, A., Leroy, P., & Maineult, A. (2019). Exploring the effect of the pore size distribution on the streaming potential generation in saturated porous media, insight from pore network simulations. *Journal of Geophysical Research: Solid Earth*, *124*, 5315–5335.

Jurin, J. (1719). Ii. an account of some experiments shown before the royal society; with an enquiry into the cause of the ascent and suspension of water in capillary tubes. *Philosophical Transactions of the Royal Society of London*, *30*, 739–747.

Katz, A. J., & Thompson, A. H. (1985). Fractal sandstone pores: Implications for conductivity and pore formation. *Phys. Rev. Lett.*, *54*, 1325–1328.

Kirby, B. (2010). *Micro and Nanoscale Fluid Mechanics: Transport in Microfluidic Devices*. Cambridge University Press.

Larue, O., Wakeman, R., Tarleton, E., & Vorobiev, E. (2006). Pressure electroosmotic dewatering with continuous removal of electrolysis products. *Chemical Engineering Science*, *61*, 4732 – 4740.

Leroy, P., & Maineult, A. (2018). Exploring the electrical potential inside cylinders beyond the DebyeHckel approximation: a computer code to solve the PoissonBoltzmann equation for multivalent electrolytes. *Geophysical Journal International*, *214*, 58–69.

Leroy, P., & Revil, A. (2004). A triple-layer model of the surface electrochemical properties of clay minerals. *Journal of Colloid and Interface Science*, *270*, 371 – 380.

Levine, S., Marriott, J., Neale, G., & Epstein, N. (1975). Theory of electrokinetic flow in fine cylindrical capillaries at high zeta-potentials. *Journal of Colloid and Interface Science*, *52*, 136 – 149.

Li, S. X., Pengra, D. B., & P.Z.Wong (1995). Onsager's reciprocal relation and the hydraulic permeability of porous media. *Physical Review E*, *51*, 5748–5751.

Liang, M., Yang, S., Miao, T., & Yu, B. (2015). Analysis of electroosmotic characters in fractal porous media. *Chemical Engineering Science*, *127*.

Liang, M., Yang, S., & Yu, B. (2014). A fractal streaming current model for charged microscale porous media. *Journal of Electrostatics*, *72*.

Linan Jiang, Mikkelsen, J., Jae-Mo Koo, Huber, D., Shuhuai Yao, Lian Zhang, Peng Zhou, Maveety, J. G., Prasher, R., Santiago, J. G., Kenny, T. W., & Goodson, K. E. (2002). Closed-loop electroosmotic microchannel cooling system for vlsi circuits. *IEEE Transactions on Components and Packaging Technologies*, *25*, 347–355.

Linde, N., Binley, A., Tryggvason, A., Pedersen, L. B., & Revil, A. (2006). Improved hydrogeophysical characterization using joint inversion of cross hole electrical resistance and ground-penetrating radar traveltime data. *Water Resources Research*, *42*.

Lockhart, N., & Hart, G. (1988). Electro-osmotic dewatering of fine suspensions: the efficacy of current interruptions. *Drying Technology*, *6*, 415–423.

Luong, D. T., & Sprik, R. (2013). Streaming potential and electroosmosis measurements to characterize porous materials. *ISRN Geophysics*, *Article ID 496352*, 8 pages.

Lyklema, J. (1995). *Fundamentals of Interface and Colloid Science*. Academic Press.

Mandelbrot, B. B. (1982). *The Fractal Geometry of Nature*. W.H. Freeman, New York.

Mohiuddin Mala, G., Li, D.-D., Werner, C., Jacobasch, H.-J., & Ning, Y. (1997). Flow characteristics of water through a microchannel between two parallel plates with electrokinetic effects. *International Journal of Heat and Fluid Flow*, *18*, 489496.

Nourbehecht, B. (1963). *Irreversible thermodynamic effects in inhomogeneous media and their applications in certain geoelectric problems*. PhD thesis, MIT Press, Cambridge, Mass, USA.

Ohshima, H., & Kondo, T. (1990). Electrokinetic flow between two parallel plates with surface charge layers: Electro-osmosis and streaming potential. *Journal of Colloid and Interface Science*, *135*, 443–448.

Olivares, W., Croxton, T. L., & McQuarrie, D. A. (1980). Electrokinetic flow in a narrow cylindrical capillary. *The Journal of Physical Chemistry*, *84*, 867–869.

Ottosen, L., & Ro¨rig-Dalgaard, I. (2006). Drying brick masonry by electroosmosis. In *Proceedings of the Seventh International Masonry Conference*. British Masonry Society.

Paillat, T., Moreau, E., P.O.Grimaud, & Touchard, G. (2000). Electrokinetic phenomena in porous media applied to soil decontamination. *IEEE Transactions on Dielectrics and Electrical Insulation*, *7*, 693–704.

Pascal, J., Oyanader, M., & Arce, P. (2012). Effect of capillary geometry on predicting electroosmotic volumetric flowrates in porous or fibrous media. *Journal of Colloid and Interface Science*, *378*, 241 – 250.

Pengra, D., Li, S. X., & Wong, P. (1999). Determination of rock properties by low frequency ac electrokinetics. *Journal of Geophysical Research*, *104*, 29485–29508.

Pride, S. (1994). Governing equations for the coupled electromagnetics and acoustics of porous media. *Physical Review B*, *50*, 15678–15696.

Pride, S. R., & Morgan, F. D. (1991). Electrokinetic dissipation induced by seismic waves. *Geophysics*, *56*, 914–925.

Quincke, G. (1861). Ueber die fortfhrung materieller theilchen durch strmende elektricitt. *Annalen der Physik*, *189*, 513–598.

Reddy, K. R., Parupudi, U. S., Devulapalli, S. N., & Xu, C. Y. (1997). Effects of soil composition on the removal of chromium by electrokinetics. *Journal of Hazardous Materials*, *55*, 135 – 158.

Reuss, F. (1809). Sur un nouvel effet de l'lectricit galvanique. *Mmoires de la Societ Imperiale de Naturalistes de Moscou*, *2*, 327–336.

Revil, A., Cathles III, L. M., & Manhardt, P. D. (1999). Permeability of shaly sands. *Water Resources Research*, *3*, 651–662.

Revil, A., & Leroy, P. (2004). Constitutive equations for ionic transport in porous shales. *Journal of Geophysical Research: Solid Earth*, *109*. B03208.

Revil, A., & Linde, N. (2006). Chemico-electromechanical coupling in microporous media. *Journal of Colloid and Interface Science*, *302*, 682 – 694.

Revil, A., Linde, N., Cerepi, A., Jougnot, D., Matthi, S., & Finsterle, S. (2007). Electrokinetic coupling in unsaturated porous media. *Journal of Colloid and Interface Science*, *313*, 315 – 327.

Rice, C., & Whitehead, R. (1965). Electrokinetic flow in a narrow cylindrical capillary. *J. Phys. Chem.*, *69*, 4017–4024.

Sen, P. N., & Goode, P. A. (1992). Influence of temperature on electrical conductivity on shaly sands. *Geophysics*, *57*, 89–96.

Singhal, V., Garimella, S. V., & Raman, A. (2004). Microscale pumping technologies for microchannel cooling systems. *Birck and NCN Publications*, *57*.

Smoluchowski, M. (1902). Contribution `a la th´eorie de l'endosmose ´electrique et de quelques ph´enom`enes corr´elatifs. *Bulletin de l'Acad´emie des Sciences de Cracovie*, *8*, 182–200.

Soldi, M., Guarracino, L., & Jougnot, D. (2019). An analytical effective excess charge density model to predict the streaming potential generated by unsaturated flow. *Geophysical Journal International*, *216*, 380–394.

Thanh, L., & Sprik, R. (2015). Zeta potential measurement using streaming potential in porous media. *VNU Journal of Science: Mathematics Physics*, *31*, 56–65.

Thanh, L. D., Jougnot, D., Van Do, P., & Van Nghia A, N. (2019). A physically based model for the electrical conductivity of water-saturated porous media. *Geophysical Journal International*, *219*, 866–876.

Thanh, L. D., Van Do, P., Van Nghia, N., & Ca, N. X. (2018). A fractal model for streaming potential coefficient in porous media. *Geophysical Prospecting*, *66*, 753–766.

Tsai, N.-C., & Sue, C.-Y. (2007). Review of mems-based drug delivery and dosing systems. *Sensors and Actuators A: Physical*, *134*, 555 – 564.

Vennela, N., Bhattacharjee, S., & De, S. (2011). Sherwood number in porous microtube due to combined pressure and electroosmotically driven flow. *Chemical Engineering Science*, *66*, 6515 – 6524.

Vinogradov, J., Jaafar, M. Z., & Jackson, M. D. (2010). Measurement of streaming potential coupling coefficient in sandstones saturated with natural and artificial brines at high salinity. *Journal of Geophysical Research*, *115*, doi:10.1029/2010JB007593.

Wang, J., Hu, H., & Guan, W. (2016). The evaluation of rock permeability with streaming current measurements. *Geophysical Journal International*, *206*, 1563–1573.

Wang, J., Hu, H., Guan, W., & Li, H. (2015). Electrokinetic experimental study on saturated rock samples: zeta potential and surface conductance. *Geophysical Journal International*, *201*, 869–877.

Wang, X., Cheng, C., Wang, S., & Liu, S. (2009). Electroosmotic pumps and their applications in microfluidic systems. *Microfluidics and Nanofluidics*, *6*, 145–162.

Wise, D. L., & Trantolo, D. J. (1994). *Remediation of Hazardous Waste Contaminated Soils*. CRC Press.

Wu, R. C., & Papadopoulos, K. D. (2000). Electroosmotic flow through porous media: cylindrical and annular models. *Colloids and Surfaces A: Physicochemical and Engineering Aspects*, *161*, 469 – 476.

Wyllie, M. R. J., & Rose, W. (1950). Some theoretical considerations related to the quantitative evaluation of the physical characteristics of reservoir rock from electrical log data. *Society of Petroleum Engineers*, .

Yao, S., & Santiago, J. G. (2003). Porous glass electroosmotic pumps: theory. *J. Colloid Interface Sci*, *268*, 133–142.

Yu, B., & Cheng, P. (2002). A fractal permeability model for bi-dispersed porous media. *International Journal of Heat and Mass Transfer*, *45*, 2983–2993.

Yu, B., Lee, L. J., & Cao, H. (2001). Fractal characters of pore microstructures of textile fabrics. *Fractals*, *09*, 155–163.

Zeng, S., Chen, C. H., Mikkelsen, J. C., & Santiago, J. G. (2001). Fabrication and characterization of electroosmotic micropumps. *Sens. Actuators B*, *79*, 107–114.